Materials Today Advances 10 (2021) 100142

Contents lists available at ScienceDirect

Materials Today Advances

journal homepage: www.journals.elsevier.com/materials-today-advances/

Ellipsometry-based failure analysis on translucent $LiMn_{0.5}Ni_{0.3}Co_{0.2}O_2$ in half-cell thin-film lithium-ion battery on glass substrates

Z. Qi [a], R. Xu [b], S. Misra [a], H. Wang [a], J. Huang [c], K. Zhao [b], H. Wang [a, *]

[a] School of Materials Engineering, Purdue University, West Lafayette, IN, 47907-2045, United States
[b] School of Mechanical Engineering, Purdue University, West Lafayette, IN, 47907-2045, United States
[c] Centre for Physical Mechanics and Biophysics, School of Materials, Sun Yat-sen University, Guangzhou, 510275, China

ARTICLE INFO

Article history:
Received 9 December 2020
Received in revised form
11 February 2021
Accepted 24 February 2021
Available online xxx

Keywords:
NMC
LIB
Cathode
Thin film
Glass substrate
Battery failure analysis

ABSTRACT

Simple one-step synthesis of $LiMn_{0.5}Ni_{0.3}Co_{0.2}O_2$ thin film on Al-doped ZnO transparent current collector has been achieved and integrated on regular glass substrates using a pulsed laser deposition technique. The crystal structure, texture properties, film morphology, and electrochemical properties are compared before and after galvanostatic cycling process. The Al-doped ZnO current collector shows excellent stability after the cycling. Simple ellipsometry measurement coupled with AFM and SEM has been successfully applied to analyze the film failure mode in the half-cell. The successful integration of the cathode on glass substrates and the application of optical-based failure analysis provide an insightful approach for potential *in operando* analysis on solid-state batteries.

1. Introduction

Thin-film lithium-ion batteries have been extensively explored owing to their great potentials as energy storage devices in portable electronics and microelectronics and the exclusion of electrochemically inactive binder. Thin-film components are also necessary in all-solid-state battery to avoid the usage of flammable organic liquid electrolyte. Currently, most of the substrates used in thin-film lithium-ion batteries are opaque conductive substrates such as metallic ones, Al-, Cu-, Ti-, and carbon-based substrates [1]. Up to date no demonstration has been made by using glass substrates.

Glass substrates are cheap and a readily available material compared with abovementioned conductive substrates and have been widely used in large flat panel displays (e.g. LED TVs and monitors) and, recently some early demonstration of integrated smart electronics and displays [2,3]. However, glass is normally insulating and a conducting transparent oxide layer is usually required, such as indium tin oxide—coated glass substrates [4–8]. Furthermore, for future integration of portable electronics directly on glass, power storage devices also need to be fully integrated. Thin-film solid-state battery integration on glass substrate could provide an effective route toward this power solution for future smart glass electronics.

Analytical operando techniques can provide pathways in exploring functionalities, operation mechanisms, and failure mechanisms, especially in a working battery. For example, magnetic resonance imaging (MRI) has been applied to monitor the Li microstructure evolution [9]. In situ high-resolution transition electron microscopy (TEM) allows similar observation at much finer scale [10]. Synchrotron X-ray technique can be used to track the strain evolution and dislocations motion in electrode particles [11]. Electron paramagnetic resonance (EPR) was used to observe strain evolution but only in paramagnetic electrodes [12]. Other techniques such as X-ray photoelectron spectroscopy (XPS), Raman, atomic force microscopy (AFM), etc., have also been studied [13]. As a complementary tool to the above analysis methods, optical-based failure analysis can provide a real-time, non-destructive approach to monitor stress evolution, fracture, film roughness, and SEI formation, etc. [14–18].

Considering the high optical transparency of glass and the great potential of optical-based failure analysis for thin film batteries, in this work, we propose to integrate a lithium-ion

* Corresponding author.
E-mail address: hwang00@purdue.edu (H. Wang).

https://doi.org/10.1016/j.mtadv.2021.100142

battery half-cell on glass substrates to demonstrate the potential in glass thin-film battery integration and optical-based battery failure analysis. The conceptual schematic of the glass-templated thin-film battery is shown in Fig. 1. Al-doped ZnO (AZO) thin film was selected as the transparent conducting oxide for the current collector, as it's optically transparent, electrically conductive, cheap, and earth-abundant [19]. Half-cells based on thin-film cathode of $LiNi_{0.5}Mn_{0.3}Co_{0.2}O_2$ (NMC 532) are integrated on the AZO-coated glass substrates. Ellipsometric optical analysis together with the scanning electron microscopy (SEM) and AFM are carried to study the failure behavior of the thin film cathodes. The results are coupled with the electrochemical performances of the half-cells to explore the underlying cathode decay mechanisms.

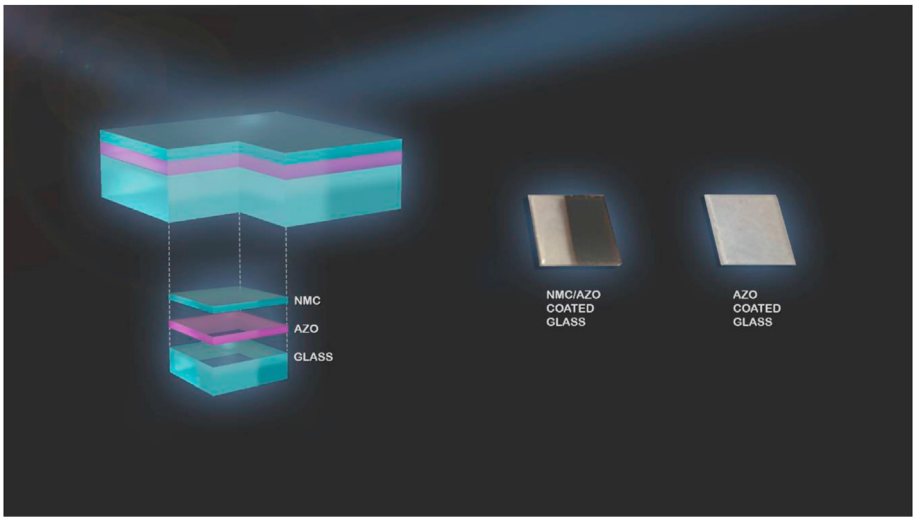

Fig. 1. Schematic drawing of the stack of cathode and current collector on glass substrates.

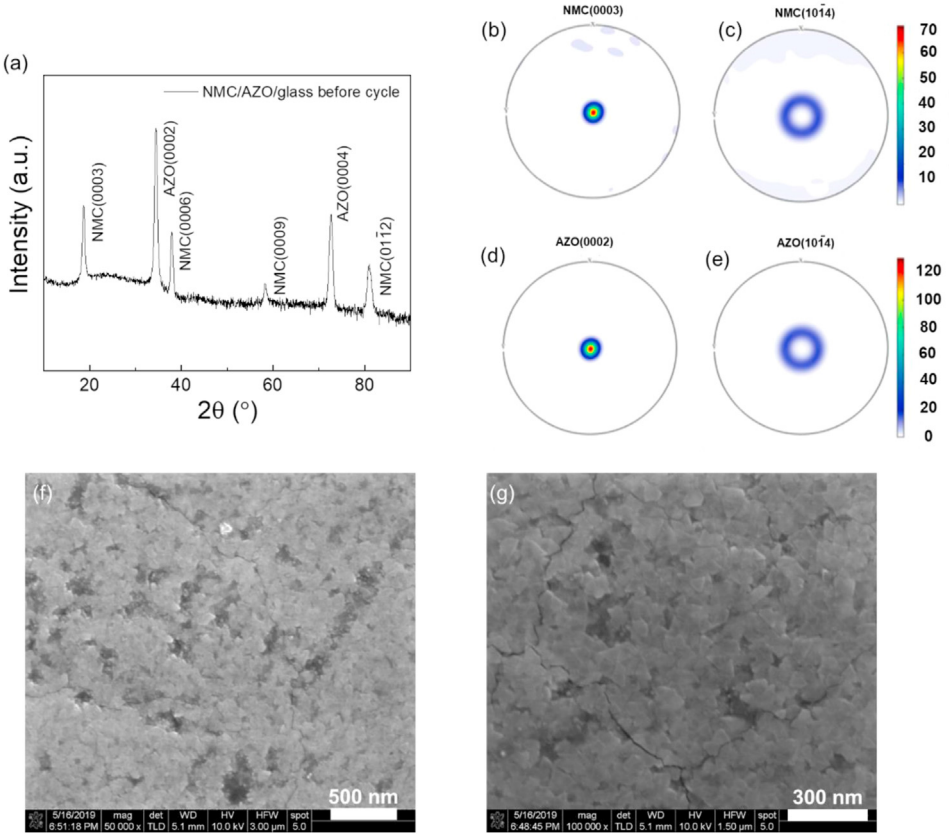

Fig. 2. (a) Out-of-plane XRD pattern of as-deposited NMC/AZO/glass thin films, (b) pole figure NMC(0003), (c) pole figure NMC(10$\bar{1}$4), (d) pole figure AZO(0002), (e) pole figure AZO (10$\bar{1}$4) of as-deposited thin films, (f) low-magnification SEM micrograph of as-deposited NMC/AZO/glass thin films, and (g) high-magnification SEM micrograph of as-deposited NMC/AZO/glass thin films.

2. Experimental

NMC532 (MTI) powder was mixed with 15% Li_2CO_3 (Alfa Aesar), cold-pressed into a pellet, and sintered at 900 °C under O_2 atmosphere for 24 hrs. More details can be found in previous reports [20,21]. Pulsed laser deposition system (Lambda Physik Compex Pro 205, 248 nm KrF) was applied for both NMC and AZO film growth. The glass substrates are regular analytical glass slides (Fisher Scientific). The target-to-substrate distance was set to 5 cm. For NMC, the growth parameters are laser frequency of 5 Hz for 33 min, energy density of 1.9 J cm^{-2}, O_2 atmosphere pressure of 10 mTorr, deposition temperature of 550 °C, and annealing at 550 °C for 1 h then cooled at10 °C/min under 15 Torr O_2. For AZO, the growth parameters are laser frequency of 10 Hz for 7 min, energy density of 3.3 J cm^{-2}, O_2 atmosphere pressure of 7 mTorr, deposition temperature at 420 °C, and cooled at 10 °C/min under 7 mTorr O_2. X-ray diffraction (XRD) was performed using PANalytical Empyrean Diffractometer system with a Cu Kα1 (λ = 1.5406 Å) source. FEI NOVA nanoSEM Field Emission was used for micrograph probe at 10 kV. Ar filled glovebox (MBraun, O_2 < 0.1 ppm, H_2O < 0.1 ppm) was used to perform two-electrode measurements with Li metal anode (Sigma Aldrich) and 1 M $LiPF_6$ in EC:DMC organic electrolyte. The setup can be found in Fig. S1, the NMC film was partially deposited onto the AZO-coated glass with exposed AZO electrode. Arbin BTS2000 testing system was used for all the electrochemical tests. The voltage window for all the measurements is between 2.0 V and 4.2 V and current was kept constant at about 5 μA/cm^2. The C-rate is estimated based on the actual measurement time for each cycle. The cyclic voltammetry (CV) was measured at potential ramp rate from 20 μV/s to 400 μV/s. The optical dielectric permittivity of all the films was evaluated using spectroscopic ellipsometry (J.A. Woollam RC2). The ellipsometer parameters ψ and Δ, related by the equation: $r_p/r_s = \tan(\psi)e^{(i\Delta)}$ (where r_p and r_s are the reflection coefficient for the p-polarization and s-polarization light, respectively) were fitted using the CompleteEASE software.

3. Results

The out-of-plane XRD measurement results are shown in Fig. 2(a). The XRD pattern shows both AZO buffer layer and NMC film with highly preferred growth orientation along the out-of-plane direction, and the lattice misfit between AZO (0002) (d = 1.36 Å) and NMC(0006) (d = 1.25 Å) can be calculated by the following equation:

$$\varepsilon_{\parallel} = \frac{|d_{NMC(0006)} - d_{AZO(0002)}|}{d_{NMC(0006)}}$$

which gives out misfit $\epsilon_{\parallel}$ around 8%. In addition, the in-plane texture property was explored using pole figure measurement exhibit in Fig. 2(b)–(e). Different from the aforementioned out-of-plane XRD pattern, the in-plane pole figures for both AZO ($10\bar{1}4$) and NMC($10\bar{1}4$) show a powder-like behavior, indicating a polycrystalline nature along the in-plane orientation. The surface morphology of the as-deposit film was first examined using SEM, as shown in Fig. 2(f) and (g). The larger-view SEM image of the as-

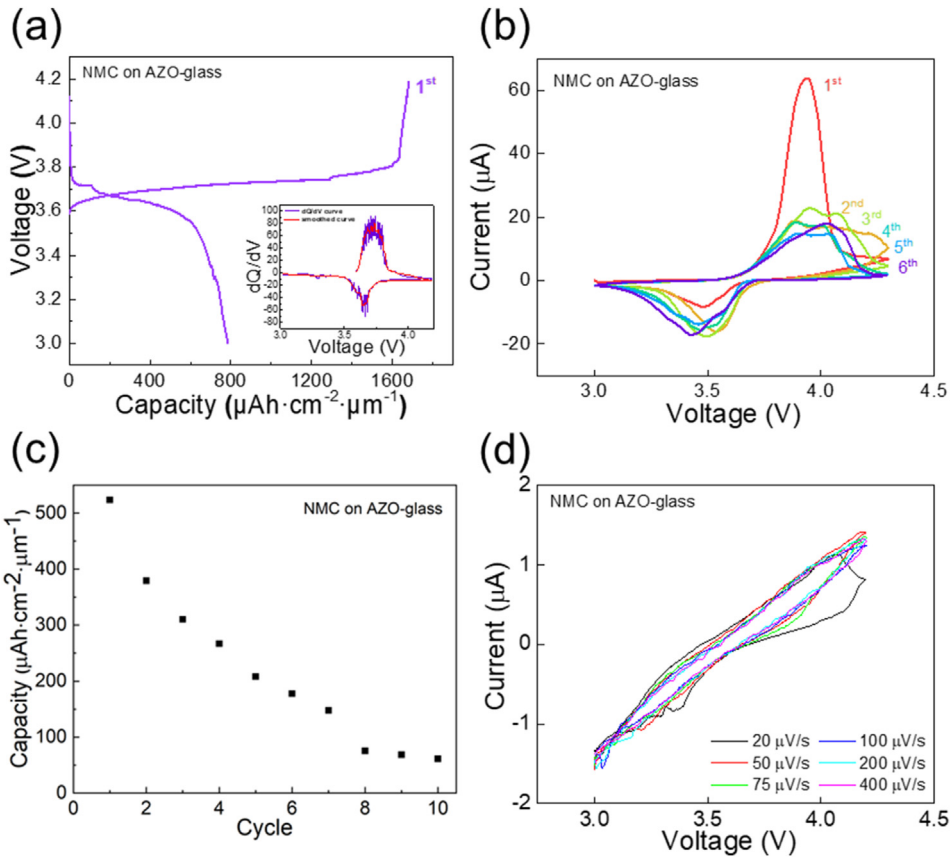

Fig. 3. (a) Charge-discharge curve of the first cycle of NMC/AZO/glass with inset showing the dQ/dV plot of that; (b) five consecutive CV cycles of NMC/AZO/glass thin films at potential sweep rate of 50 μV/s; (c) cycling behavior of NMC/AZO/glass thin films for 10 cycles; (d) CV measurements of NMC/AZO/glass after cycles at different sweep rate of 20 μV/s, 50 μV/s, 75 μV/s, 100 μV/s, 200 μV/s, and 400 μV/s.

deposited thin film is shown in Fig. S4(a). It exhibits a typical platelet grain morphology of layered oxides obtained by pulsed laser deposition, very similar to prior reported surface morphology [22]. Besides, some minor cracks can be observed along the grain boundaries. The possible reasons for this can be a result of strain relaxation from the large mismatch between the preferred orientation of AZO current collectors and NMC films [23–25], which are calculated above.

The electrochemical measurements were conducted using a two-electrode setup in the glovebox. The thin-film cathode was cycled between 3.0 V and 4.2 V galvanostatically and the charge rate can be estimated to be around 0.02C while the discharge rate is roughly 0.05C for the first cycle in Fig. 3(a). The discharge capacity is about 800 μAh cm^{-2} μm^{-1}, which exceeds the theoretical volumetric capacity of 574.08 μAh cm^{-2} μm^{-1} and this suggests heavy pseudocapacitive contribution from the thin film nature as we believe the extra capacity contribution is from the electric double-layer capacitor characteristics and the electrolyte species [26]. The possible electrolyte decomposition can be excluded as the dQ/dV plot shown in the inset only shows the typical anodic and cathodic peaks of Ni^{2+}/Ni^{4+} pairs [27]. Five consecutive cycles of CV measurements were performed at ramp rate of 50 μV/s in Fig. 3(b). The average potential of cathodic peaks is around 3.5 V and that of anodic peaks is 3.95 V, representing $Ni^{4+} \rightarrow Ni^{2+}$ reduction reactions and $Ni^{2+} \rightarrow Ni^{4+}$ oxidation reactions, respectively. The relatively large potential difference between anodic and cathodic reactions suggests a significant polarization in the cathode, which is expected due to the thin-film properties of the as-deposited NMC. It is also noted the intensity ratio of cathodic peaks to anodic peaks largely increased after the first cycle, indicating the improved redox reaction reversibility after full activation and homogenization. The galvanostatic cycling test shows the capacity decays fast in 10 cycles, and the C-rate at the 10th cycle is about 2.6C where the 1st cycle has C-rate about 0.3C in Fig. 3(c). The CV measurements were again applied on the cycled film, shown in Fig. 3(d), and it shows pure pseudocapacitive behavior under different ramp rates, and the distortion is due to diffusion limit and is small [28,29].

The cycled film was cleaned and the structure as well as surface morphology were remeasured using XRD and SEM. The out-of-plane XRD of the cycled film is shown in Fig. 4(a), which is observed that the peak intensities of NMC are largely decreased while that of AZO almost stays the same. The overlayered plots are shown in Fig. S2, and only NMC(0003) peak is shown after cycling as the reduction of crystallinity diminishes the high-order peaks that has lower intensities. Similar trend can be derived from the pole figure results in Fig. 4(b)–(e). The NMC(0003) pole show reduced out-of-plane intensity and more randomized orientation distribution, suggesting possible fragmentation or mechanical failure of cycled film. However, the AZO pole figures almost have no difference compared with that of the as-deposited AZO. The SEM micrographs in Fig. 4(f) and (g) confirm the mechanical failure, where the cracks along the grain boundaries have propagated significantly and some intragranular cracks can also be observed in the high-mag SEM micrograph. The larger-view SEM image of the cycled thin film is shown in Fig. S4(b). Nonetheless, no obvious film delamination is observed.

The uncycled and cycled thin films were further optically characterized using spectroscopic ellipsometer. A linearly polarized

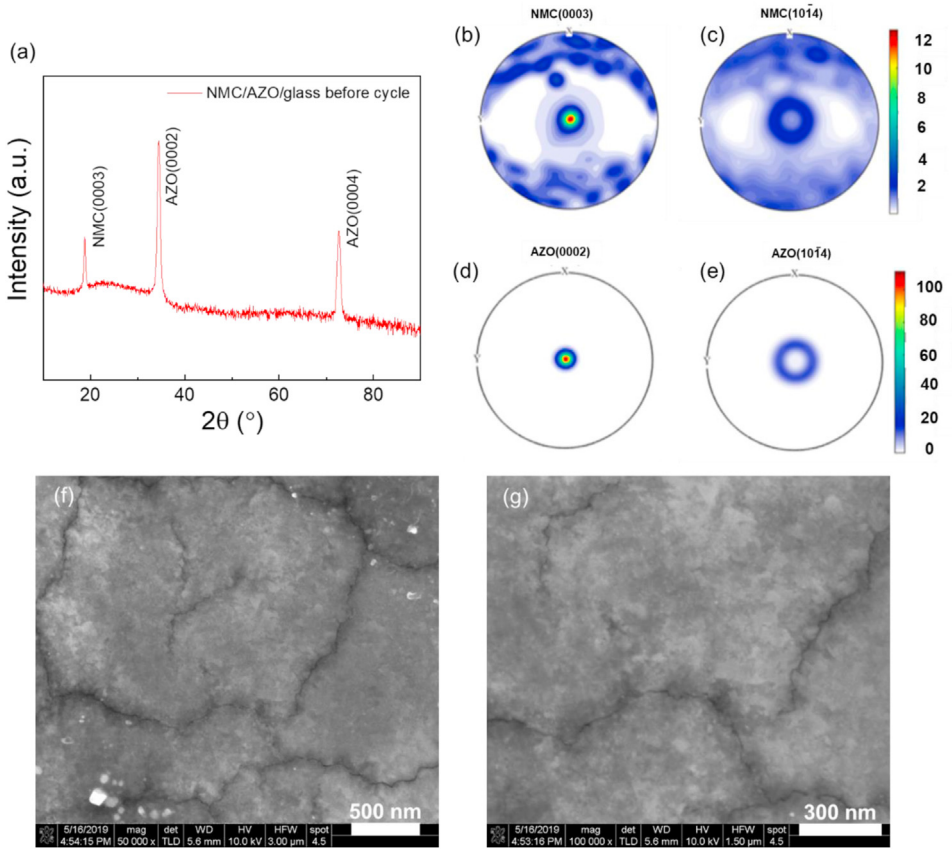

Fig. 4. (a) Out-of-plane XRD pattern of cycled NMC/AZO/glass thin films, (b) pole figure NMC(0003), (c) pole figure NMC(10$\bar{1}$4), (d) pole figure AZO(0002), (e) pole figure AZO (10$\bar{1}$4) of cycled thin films, (f) low-magnification SEM micrograph of cycled NMC/AZO/glass thin films, and (g) high-magnification SEM micrograph of cycled NMC/AZO/glass thin films.

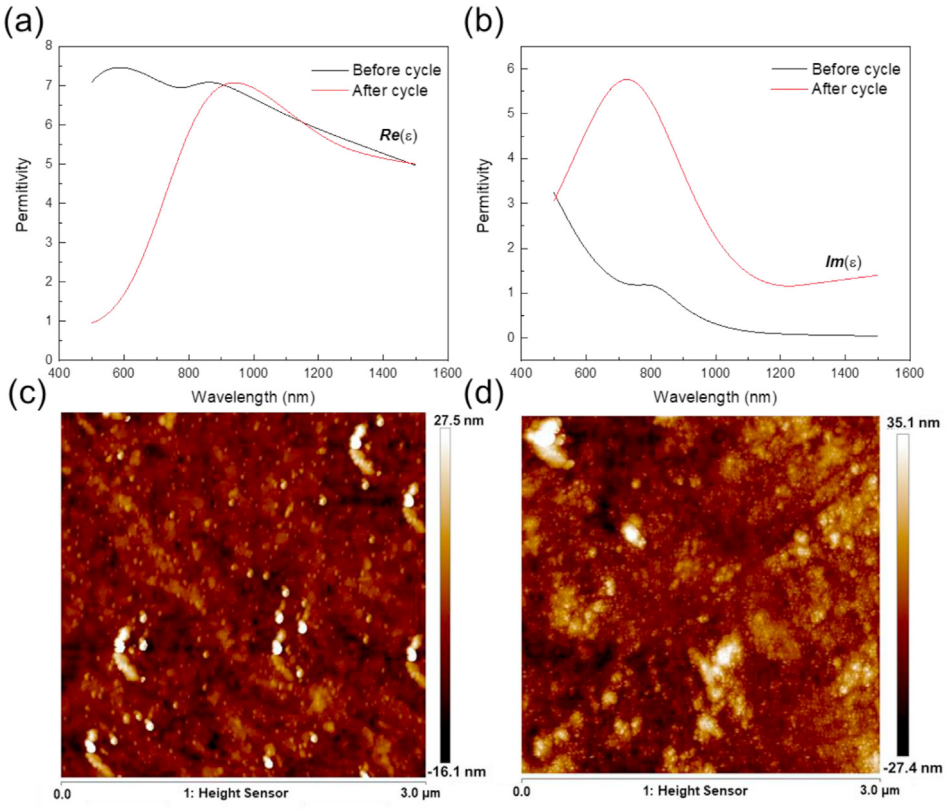

Fig. 5. (a) Real parts and (b) imaginary parts comparison of permittivity curves for NMC/AZO/glass thin films before and after cycling; the AFM surface mappings of NMC/AZO/glass thin films (c) before cycling and (d) after cycling showing roughened surface due to electrochemical cycling.

light was incident onto the NMC/AZO/glass stack and the reflected light was collected for analysis. The ellipsometric parameters ψ and Δ, measured at three different incident angles (55°, 65°, and 75°) is shown in Fig. S3. At the 75° incidence angle, a sudden change in Δ can be seen in the uncycled sample. This sudden jump shows a red shift and becomes weaker for the cycled sample. This change in the ψ and Δ can be attributed to the development of cracks within the film as has been reported previously [16], which matches with the SEM result. Furthermore, the ψ and Δ parameters were modeled using a three-layer isotropic model consisting of the NMC thin film, the AZO current collector, and the glass substrate. The thickness of the layers was calculated using STEM images and provided as an input to the model. AZO layer was modeled using a Drude-Lorentz oscillator while the NMC layer was modeled using a Lorentz and Tauc-Lorentz oscillator. The permittivity of the AZO layer was assumed to be constant during the fitting. Fig. 5(a) and (b) show the calculated permittivity of the NMC film for the uncycled and cycled state. Clearly, the permittivity shows a red-shift upon cycling the sample. Furthermore, the AFM surface mappings in Fig. 5(c) and (d) demonstrate a roughened surface of NMC thin films due to the electrochemical cycling. Such change of the film can be related to CEI formation and the heterogenous damage during cycling at the coherent interface of NMC and AZO [17,30].

4. Discussion

This work has demonstrated the possibility of electrode integration on glass substrates. However, the electrochemical performance is not satisfying due to the unideal current collector, and this could be potentially resolved by selecting other transparent conducting oxides or nontransparent Au metallic current collectors. This is the next-step progress before the full-cell integration could be realized on glass substrate, which will have to introduce solid state electrolyte (SSE). In addition, owing to the commonly lower ionic conductivity of SSE compared with organic liquid electrolyte as well as the prevailing interfacial instability, electrode modification also needs to be practiced.

Furthermore, the ellipsometry measurements demonstrated an optical-based failure analysis method. This technique is less dependent on hardware compared with other techniques which require either special designed cell or medium- to large-scale complex equipment such as AFM, EPR, MRI, XPS, etc., mentioned in the introduction section, and such easy accessible detection method is highly appreciated as *in-operando* technique. In addition, this technique collects more information than multibeam optical stress sensor technique, which only reflects mechanical information. However, systematic study will be carried out on NMC cathode at different failure modes and stages to correlate them with different ellipsometric response.

5. Conclusions

In this work, translucent NMC thin film on AZO-coated transparent glass substrate as a half-cell structure has been successfully demonstrated for optical-based failure analysis. The film integrated on AZO-buffered glass shows a rapidly decayed electrochemical performance upon cycling. The primary failure mechanism is the formation of cracks due to the large lattice mismatch between the NMC film and the AZO buffer. This is confirmed from the ellipsometry result by the red shift and reduced dielectric properties in the ellipsometric measurement results, and also consistent with the surface morphologies observed from SEM and AFM. This

demonstration of thin film battery integrated on glass substrates paves a path toward future integrated power sources for smart glass integrated electronics and provides a non-destructive method for *in situ* monitoring of all-solid-state lithium-ion batteries.

Credit author statement

Zhimin Qi, Conceptualization, Methodology, Data acquisition, Writing, Reviewing and Editing. Rong Xu, Assisted Electrochemical data acquisition. Shikhar Misra, Ellipsometry data acquisition and Formal analysis. Han Wang, Assisted TEM data acquisition. Jijie Huang, Results discussion, reviewing and editing. Kejie Zhao, Results discussion, reviewing and editing, Haiyan Wang, Supervision, reviewing and editing.

Data availability

The raw data required to reproduce these findings are available to download from https://doi.org/10.17632/hnxt465s6c.1. The processed data required to reproduce these findings are available to download from https://doi.org/10.17632/jvrgstpfws.1.

Declaration of competing interest

The authors declare that they have no known competing financial interests or personal relationships that could have appeared to influence the work reported in this paper.

Acknowledgements

This work is partially supported by the U.S. Office of Naval Research (ONR, N00014-20-1-2600). The high-resolution TEM/STEM characterization at Purdue University is supported by the U.S. National Science Foundation (DMR-2016453).

Appendix A. Supplementary data

Supplementary data to this article can be found online at https://doi.org/10.1016/j.mtadv.2021.100142.

References

[1] Z. Qi, H. Wang, Advanced thin film cathodes for lithium ion batteries, Research 2020 (2020) 1–24, https://doi.org/10.34133/2020/2969510.
[2] J. Jiang, J.P. Liu, X.T. Huang, Y.Y. Li, R.M. Ding, X.X. Ji, Y.Y. Hu, Q.B. Chi, Z.H. Zhu, General synthesis of large-scale arrays of one-dimensional nanostructured Co3O4 directly on heterogeneous substrates, Cryst. Growth Des. 10 (2010) 70–75, https://doi.org/10.1021/cg9001835.
[3] Umm-e-Farwa, K.S. Ahmad, Z. Hussain, S. Majid, Synthesis, characterization and PVD assisted thin film fabrication of the nano-structured bimetallic Ni3S2/MnS2 composite, Surf Interfaces 12 (2018) 190–195, https://doi.org/10.1016/j.surfin.2018.06.003.
[4] B.J. Hwang, C.Y. Wang, M.Y. Cheng, R. Santhanam, Structure, morphology, and electrochemical investigation of LiMn 2O 4 thin film cathodes deposited by radio frequency sputtering for lithium microbatteries, J. Phys. Chem. C 113 (2009) 11373–11380, https://doi.org/10.1021/jp810881d.
[5] H. Otsuji, K. Kawahara, T. Ikegami, K. Ebihara, LiMn2O4 thin films prepared by pulsed laser deposition for rechargeable batteries, Thin Solid Films 506–507 (2006) 120–122, https://doi.org/10.1016/j.tsf.2005.08.126.
[6] N. Ibris, A.M. Salvi, M. Liberalore, F. Decker, A. Surca, XPS study of the Li intercalation process in sol-gel-produced v 2O5 thin film: influence of substrate and film synthesis modification, Surf. Interface Anal. 37 (2005) 1092–1104, https://doi.org/10.1002/sia.2084.
[7] Y. Zeng, G. Gao, G. Wu, H. Yang, Nanosheet-structured vanadium pentoxide thin film as a carbon- and binder-free cathode for lithium-ion battery applications, J. Solid State Electrochem. 19 (2015) 3319–3328, https://doi.org/10.1007/s10008-015-2941-5.
[8] J.D. Perkins, C.S. Bahn, J.M. McGraw, P.A. Parilla, D.S. Ginley, Pulsed laser deposition and characterization of crystalline lithium cobalt cioxide (LiCoO [sub 2]) thin films, J. Electrochem. Soc. 148 (2002) A1302, https://doi.org/10.1149/1.1415029.
[9] S. Chandrashekar, N.M. Trease, H.J. Chang, L.S. Du, C.P. Grey, A. Jerschow, 7Li MRI of Li batteries reveals location of microstructural lithium, Nat. Mater. 11 (2012) 311–315, https://doi.org/10.1038/nmat3246.
[10] F. Wang, H.C. Yu, M.H. Chen, L. Wu, N. Pereira, K. Thornton, A. Van Der Ven, Y. Zhu, G.G. Amatucci, J. Graetz, Tracking lithium transport and electrochemical reactions in nanoparticles, Nat. Commun. 3 (2012) 1–8, https://doi.org/10.1038/ncomms2185.
[11] U. Ulvestad, A. Singer, J.N. Clark, H.M. Cho, J.W. Kim, R. Harder, J. Maser, Y.S. Meng, O.G. Shpyrko, Topological defect dynamics in operando battery nanoparticles, Science (80-.) 348 (2015) 1344–1347, https://doi.org/10.1126/science.aaa1313.
[12] M. Sathiya, J.B. Leriche, E. Salager, D. Gourier, J.M. Tarascon, H. Vezin, Electron paramagnetic resonance imaging for real-time monitoring of Li-ion batteries, Nat. Commun. 6 (2015) 1–7, https://doi.org/10.1038/ncomms7276.
[13] C.P. Grey, J.M. Tarascon, Sustainability and in situ monitoring in battery development, Nat. Mater. 16 (2016) 45–56, https://doi.org/10.1038/nmat4777.
[14] J. Lei, L. Li, R. Kostecki, R. Muller, F. McLarnon, Characterization of SEI layers on LiMn[sub 2]O[sub 4] cathodes with in situ spectroscopic ellipsometry, J. Electrochem. Soc. 152 (2005) A774, https://doi.org/10.1149/1.1867652.
[15] J. Duay, K.W. Schroder, S. Murugesan, K.J. Stevenson, Monitoring volumetric changes in silicon thin-film anodes through in situ optical diffraction microscopy, ACS Appl. Mater. Interfaces 8 (2016) 17642–17650, https://doi.org/10.1021/acsami.6b03822.
[16] M. Pharr, Z. Suo, J.J. Vlassak, Measurements of the fracture energy of lithiated silicon electrodes of Li-Ion batteries, Nano Lett. 13 (2013) 5570–5577, https://doi.org/10.1021/nl403197m.
[17] R. Greef, Ellipsometry in electrochemistry: a spectrum of applications, Thin Solid Films 233 (1993) 32–39, https://doi.org/10.1016/0040-6090(93)90056-U.
[18] V.A. Sethuraman, M.J. Chon, M. Shimshak, V. Srinivasan, P.R. Guduru, In situ measurements of stress evolution in silicon thin films during electrochemical lithiation and delithiation, J. Power Sources 195 (2010) 5062–5066, https://doi.org/10.1016/j.jpowsour.2010.02.013.
[19] N.F. Shih, J.Z. Chen, Y.L. Jiang, Properties and analysis of transparency conducting AZO films by using DC power and RF power simultaneous magnetron sputtering, Adv. Mater. Sci. Eng. 2013 (2013) 1–7, https://doi.org/10.1155/2013/401392.
[20] Z. Qi, J. Jian, J. Huang, J. Tang, H. Wang, V.G. Pol, H. Wang, $LiNi_{0.5}Mn_{0.3}Co_{0.2}O_2$/Au nanocomposite thin film cathode with enhanced electrochemical properties, Nano Energy 46 (2018) 290–296, https://doi.org/10.1016/j.nanoen.2018.02.011.
[21] Z. Qi, J. Tang, J. Huang, D. Zemlyanov, V.G. Pol, H. Wang, Li2MnO3 thin films with Tilted tomain structure as cathode for Li-ion batteries, ACS Appl. Energy Mater. 2 (2019) 3461–3468, https://doi.org/10.1021/acsaem.9b00259.
[22] J.C. Garcia, J. Bareño, J. Yan, G. Chen, A. Hauser, J.R. Croy, H. Iddir, Surface structure, morphology, and stability of $Li(Ni_{1/3}Mn_{1/3}Co_{1/3})O_2$ cathode material, J. Phys. Chem. C 121 (2017) 8290–8299, https://doi.org/10.1021/acs.jpcc.7b00896.
[23] R. Koerver, W. Zhang, L. De Biasi, S. Schweidler, A.O. Kondrakov, S. Kolling, T. Brezesinski, P. Hartmann, W.G. Zeier, J. Janek, Chemo-mechanical expansion of lithium electrode materials-on the route to mechanically optimized all-solid-state batteries, Energy Environ. Sci. 11 (2018) 2142–2158, https://doi.org/10.1039/c8ee00907d.
[24] A. Chen, Q. Su, H. Han, E. Enriquez, Q. Jia, Metal oxide danocomposites: a nerspective from strain, defect, and interface, Adv. Mater. (2018) 1–30, https://doi.org/10.1002/ADMA.201803241, 1803241.
[25] W. Zhang, A. Chen, Z. Bi, Q. Jia, J.L. Macmanus-Driscoll, H. Wang, Interfacial coupling in heteroepitaxial vertically aligned nanocomposite thin films: from lateral to vertical control, Curr. Opin. Solid State Mater. Sci. 18 (2014) 6–18, https://doi.org/10.1016/j.cossms.2013.07.007.
[26] Y. Gogotsi, R.M. Penner, Energy storage in nanomaterials – capacitive, pseudocapacitive, or battery-like? ACS Nano 12 (2018) 2081–2083, https://doi.org/10.1021/acsnano.8b01914.
[27] Z. Liu, A. Yu, J.Y. Lee, Synthesis and characterization of LiNi1-x-yCoxMnyO2 as the cathode materials of secondary lithium batteries, J. Power Sources 81–82 (1999) 416–419.
[28] V. Augustyn, J. Come, M.A. Lowe, J.W. Kim, P.L. Taberna, S.H. Tolbert, H.D. Abruña, P. Simon, B. Dunn, High-rate electrochemical energy storage through Li^+ intercalation pseudocapacitance, Nat. Mater. 12 (2013) 518–522, https://doi.org/10.1038/nmat3601.
[29] Y. Xia, T.S. Mathis, M.Q. Zhao, B. Anasori, A. Dang, Z. Zhou, H. Cho, Y. Gogotsi, S. Yang, Thickness-independent capacitance of vertically aligned liquid-crystalline MXenes, Nature 557 (2018) 409–412, https://doi.org/10.1038/s41586-018-0109-z.
[30] R. Xu, Y. Yang, F. Yin, P. Liu, P. Cloetens, Y. Liu, F. Lin, K. Zhao, Heterogeneous damage in Li-ion batteries: cxperimental analysis and theoretical modeling, J. Mech. Phys. Solids 129 (2019) 160–183, https://doi.org/10.1016/j.jmps.2019.05.003.